nature nanotechnology

LETTERS

PUBLISHED ONLINE: 23 JANUARY 2011 | DOI: 10.1038/NNANO.2010.282

Plasmonic Luneburg and Eaton lenses

Thomas Zentgraf[1†], Yongmin Liu[1†], Maiken H. Mikkelsen[1†], Jason Valentine[1,2] and Xiang Zhang[1,3*]

Plasmonics takes advantage of the properties of surface plasmon polaritons, which are localized or propagating quasi-particles in which photons are coupled to the quasi-free electrons in metals. In particular, plasmonic devices can confine light in regions with dimensions that are smaller than the wavelength of the photons in free space, and this makes it possible to match the different length scales associated with photonics and electronics in a single nanoscale device[1]. Broad applications of plasmonics that have been demonstrated to date include biological sensing[2], sub-diffraction-limit imaging, focusing and lithography[3–5] and nano-optical circuitry[6–10]. Plasmonics-based optical elements such as waveguides, lenses, beamsplitters and reflectors have been implemented by structuring metal surfaces[7,8,11,12] or placing dielectric structures on metals[6,13–15] to manipulate the two-dimensional surface plasmon waves. However, the abrupt discontinuities in the material properties or geometries of these elements lead to increased scattering of surface plasmon polaritons, which significantly reduces the efficiency of these components. Transformation optics provides an alternative approach to controlling the propagation of light by spatially varying the optical properties of a material[16,17]. Here, motivated by this approach, we use grey-scale lithography to adiabatically tailor the topology of a dielectric layer adjacent to a metal surface to demonstrate a plasmonic Luneburg lens that can focus surface plasmon polaritons. We also make a plasmonic Eaton lens that can bend surface plasmon polaritons. Because the optical properties are changed gradually rather than abruptly in these lenses, losses due to scattering can be significantly reduced in comparison with previously reported plasmonic elements.

Transformation optics is a general approach to optical design in which the required optical path and functionality are achieved by spatially varying the optical properties of materials, which is in contrast to the traditional methods of shaping the surface curvature of objects (such as lenses) to refract light. Early transformation optics devices, such as the electromagnetic cloak[18], generally required spatial variation of anisotropic materials and extreme values for both permittivity and permeability. Although such demanding material properties can be implemented with metamaterials, the narrow bandwidth and high losses normally associated with metamaterials limits the functionalities of the devices. Great efforts have therefore been made in realizing new transformation optics devices based on non-resonant and isotropic materials with spatially varying properties. Examples include the carpet cloak[19,20], the photonic black hole[21], the optical 'Janus' device[22] and the flattened Luneburg lens[23]. The development of such devices and elements is essentially based on gradient index (GRIN) optics. Compared with classical lenses, GRIN lenses have an advantage in that they can be flat and free of geometrical aberrations. In fact, based on variable refractive index structures, more sophisticated elements like the Maxwell fish-eye lens, the Luneburg lens and the Eaton lens were proposed more than half a century ago[24,25], but have not been demonstrated in three-dimensional optics to date.

Recently, it has been proposed that transformation optics can be applied to plasmonic systems, aiming to manipulate the propagation of surface plasmon polaritons (SPPs) in a prescribed manner[26–29]. If we rigorously follow the transformation optics approach, both the metal and the dielectric have to undergo a coordinate transformation to modify the propagation of SPPs. However, as most SPP energy resides in the dielectric medium would be frequencies away from the surface plasmon frequency, it was proposed that transforming only the dielectric medium would be sufficient to mould the propagation of SPPs[26,27]. Furthermore, the transformed dielectric materials can be isotropic and non-magnetic if a prudent transformation scheme is applied. Instead of directly modifying the permittivity of the dielectric medium, we have proposed slowly changing the thickness of an isotropic dielectric cladding layer, and hence the local effective index of SPPs[27]. In such a way, the propagation of SPPs can be controlled without directly modifying the metal surface or adding discrete scattering structures on the metal. Because the local effective index of SPPs is varied gradually in a truly continuous manner, we term our approach GRIN plasmonics, in analogy to the well-known GRIN optics.

Here we demonstrate a plasmonic Luneburg lens and a plasmonic Eaton lens as a proof of principle of GRIN plasmonics. Both lenses require a gradual change of the mode index, which in general is difficult to obtain in traditional optical elements. The plasmonic Luneburg lens (Fig. 1a) is similar to a traditional Luneburg lens[24] in that it focuses SPPs to a point on the perimeter of the lens. The concept of the Luneburg lens was later generalized by Eaton[25] for spherical lenses. As shown later, such lenses can lead to beam deflection[30]. Both structures for the propagation of SPPs by spatially varying the height of a thin dielectric ($\varepsilon = 2.19$) poly(methyl methacrylate) (PMMA) film on top of a gold surface.

The index distribution of a traditional Luneburg lens satisfies the expression

$$n(r) = \sqrt{2 - (r/R)^2} \qquad (1)$$

where R is the radius of the lens and r the distance to the centre. To implement a plasmonic version of the Luneburg lens, the effective mode index of the SPPs should vary spatially according to equation (1). For a lens diameter of 13 μm this leads to the mode index profile shown in Fig. 1b. Changing the height of a dielectric cladding layer is a simple way to modify the effective index of the SPPs[27]. At a wavelength of 810 nm, the effective mode index of SPPs on a gold film can be changed from 1.02 to 1.54 as the height of the PMMA increases from zero to 500 nm (see Fig. 1c and Methods). Once the relationship between the SPP effective index and the PMMA height is known, the height profile for the Luneburg lens can be readily interpolated to satisfy equation (1).

[1]NSF Nanoscale Science and Engineering Center (NSEC), 3112 Etcheverry Hall, University of California, Berkeley, California 94720, USA, [2]Department of Mechanical Engineering, Vanderbilt University, Nashville, Tennessee 37235, USA, [3]Materials Science Division, Lawrence Berkeley National Laboratory, 1 Cyclotron Road, Berkeley, California 94720, USA; †These authors contributed equally to this work. *e-mail: xiang@berkeley.edu

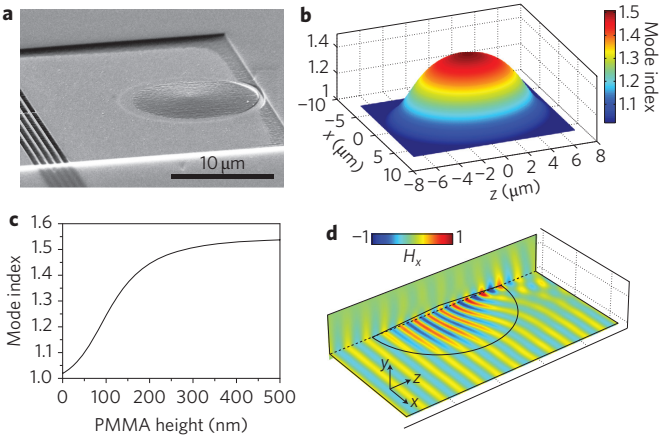

Figure 1 | Plasmonic Luneburg lens. a, SEM image of a Luneburg lens made of PMMA on top of a gold film (lens diameter, 13 μm). The grating for the SPPs (left) is made of air grooves fabricated by focused ion beam milling. **b**, Mode index (vertical axis) for the Luneburg lens at a wavelength of 810 nm. **c**, Relation between PMMA height and mode index for SPPs on a gold surface at a wavelength of 810 nm. **d**, Cross-sections of the normalized magnetic field H_x (at the metal–dielectric interface in the x–z plane and for $x = 0$ in the y–z plane) for SPPs propagating through the Luneburg lens in the positive z-direction. The lens is designed to focus the SPPs to a point on the perimeter of the lens.

Based on the local height profile of the PMMA structure measured by atomic force microscopy (AFM), we performed an additional three-dimensional full wave simulation (COMSOL Multiphysics) to verify the theoretical performance of the Luneburg lens. The result is shown in Fig. 1d, where SPPs launched from the left-hand side can indeed be focused to a point on the perimeter of the dielectric cone base. In addition, the gradual change of the mode index (impedance matching) reduces the scattering loss of SPPs and the reflections from element boundaries inherent to discrete structured elements by at least one order of magnitude.

Grey-scale electron beam lithography (EBL) was used to spatially vary the PMMA height profile. In this manner, the electron dose is continually varied across the sample to modulate the height of the PMMA layer and thus the mode index of SPPs. Fluorescence imaging[31] and leakage radiation microscopy[32] were applied to characterize the performance of the lenses (see Methods).

The investigation began with fluorescence imaging of SPP propagation in the Luneburg lens. SPPs at 810 nm were launched with a grating coupler at a distance of 10 μm from the lens structure. Simultaneously, the fluorescence of the incorporated dye molecules in the PMMA excited by the SPPs was imaged on a camera to visualize SPP propagation. Figure 2 shows fluorescence images that were obtained for SPPs passing the Luneburg lens at different positions. To demonstrate that the propagation of the SPPs was modified as required after passing the lens structure, the PMMA behind the lens (along the SPP propagation direction) was not removed, allowing us to observe the light path of the SPPs after the focal point with the fluorescence emission. As the SPPs enter the area of the Luneburg lens (dashed circle) they are focused to a point on the perimeter of the lens on the opposite side. Even if the position of the incident SPPs is changed laterally, the SPPs are still focused to the same spot (Fig. 2). Because the dyes are excited by the evanescent field of the SPPs penetrating the PMMA, the local fluorescence intensity depends not only on the strength of the SPPs but also on the thickness of the PMMA at that location. We therefore calculated the corresponding fluorescence emission by integrating the field strength of the evanescent field over the thickness of the structures to compare ideal SPP propagation with the measured fluorescence images (lower panels in Fig. 2). Agreement between the experimental results and numerical calculations for the ideal structure is very good. The slight shadows in the measured fluorescence images are probably due to non-uniformity in the dye concentration and surface defects in the PMMA layer.

Because visualization of the entire SPP beam path along the surface was not accessible using this technique, we used leakage radiation microscopy to image SPP propagation on the metal–air interface. For this investigation, a second set of samples was fabricated on a 50 nm gold film on top of a 150 μm glass substrate. Owing to the reduced thickness of the metal film, SPPs from the top interface can couple through the film and generate a coherent leakage radiation into the higher index substrate[32]. For these samples, no dyes were incorporated into the PMMA. Despite the difference in thickness of the gold film, no appreciable difference in the SPP propagation constant was found between the two configurations. However, imaging the leakage radiation from the back side of the substrate provided a direct quantitative analysis of the SPP propagation on the top metal surface.

Typical leakage radiation images recorded for SPPs at different wavelengths propagating through a Luneburg lens are shown in Fig. 3a–c, each exhibiting a characteristic fringe pattern arising from the interference of the directly transmitted light and the leakage radiation of the SPPs. Because of the laser light coherence, such interference fringes can give some information about the phase evolution of the SPPs while propagating along the surface. The phase front appears flat when launched at the grating and starts curving inside the lens, leading to focusing at a point on the perimeter, consistent with the full-wave simulation shown in Fig. 1d. The mode index of the SPPs at the centre of the Luneburg lens approaches the light cone for propagating waves at the glass substrate side ($n = 1.5$). This leads to a decrease of the leakage radiation that can be collected by the numerical aperture

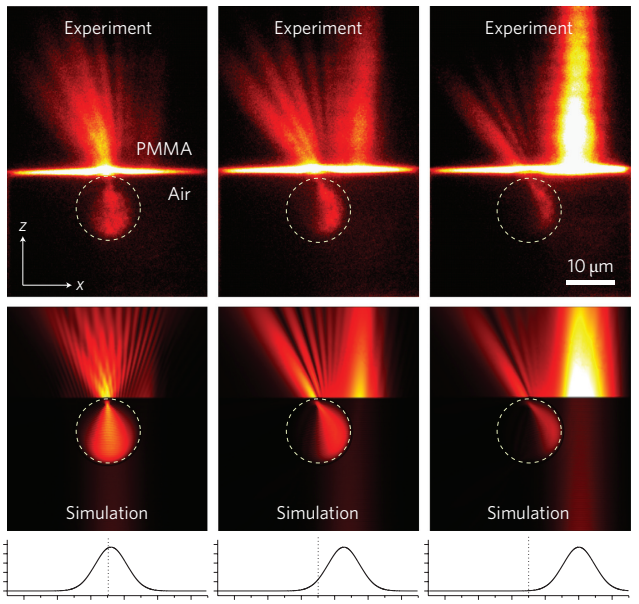

Figure 2 | Fluorescence images of a plasmonic Luneburg lens. Fluorescence intensity for SPPs passing through the Luneburg lens (upper panels) and corresponding simulations (lower panels). Fluorescence intensity is colour-coded from black (low) to white (high). Positions of lenses are marked by the yellow dotted circle. SPPs have a Gaussian intensity distribution along the x axis with a full-width at half-maximum of 6 μm. The images show propagation of SPPs in the positive z-direction for three different launching positions in the x-direction, as indicated by the beam profile below the images (vertical dotted line marks the centre of the lens).

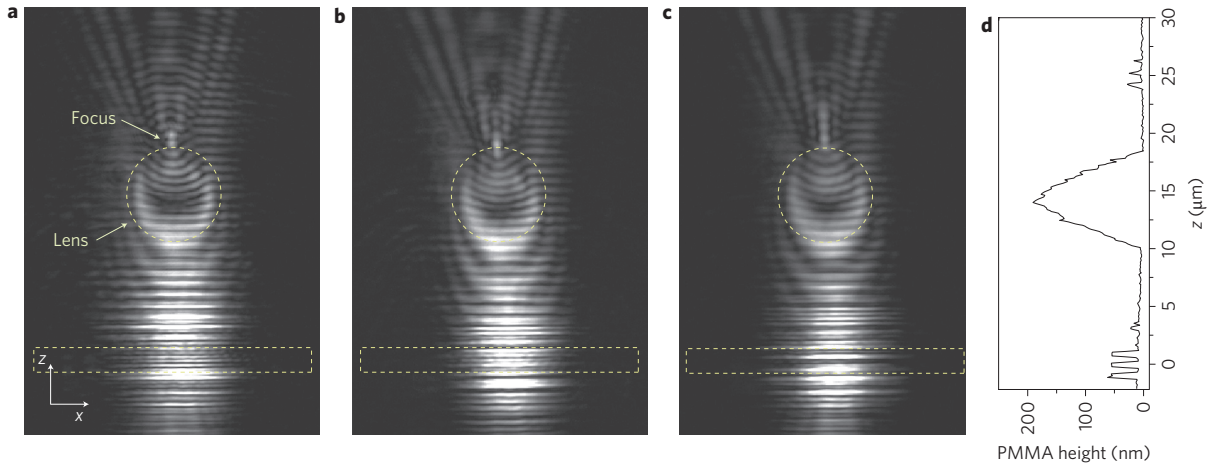

Figure 3 | Broadband performance of a plasmonic Luneburg lens. a–c, Intensity images obtained by leakage radiation microscopy for SPPs passing a Luneburg lens for wavelengths of 770 nm (**a**), 800 nm (**b**) and 840 nm (**c**). These images show focusing over a 70 nm bandwidth for the plasmonic Luneburg lens. SPPs are launched from a gold grating (dashed box) towards the Luneburg lens (dashed circle), which is 10 μm from the grating. **d**, Corresponding surface profile cross-section along the propagation (z) direction measured by AFM, showing the height of the lens and the gratings.

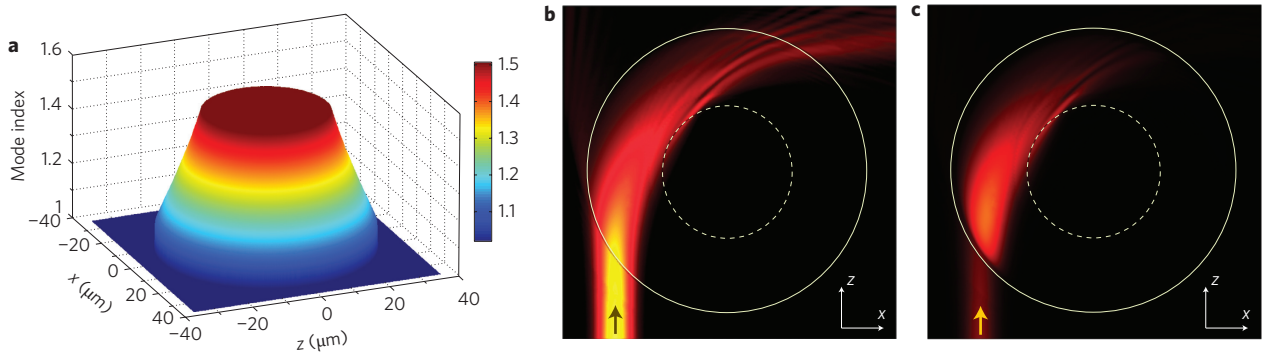

Figure 4 | Numerical simulations of a plasmonic Eaton lens. a, Truncated mode index profile for an Eaton lens with a radius of 30 μm. Values larger than 1.54 in the centre are cut and set to 1.54 due to the finite range provided by the index of SPPs at the metal–PMMA interface. **b**, Calculated magnitude of the electric surface field for a SPP launched in the positive z-direction. The solid line marks the outer diameter of the lens, and the dashed line marks the truncated index region with values set to 1.54. The SPPs bend to the right side when passing through the lens. **c**, Calculated fluorescence intensity for **b**, taking the height of the dye/PMMA layer into account, visualizing the expected intensity from the structure. In the colour scale in **b** and **c**, black represents low field amplitudes/intensities and yellow indicates high field amplitudes/intensities.

of the microscope objective. The imaged intensity inside the Luneburg lens is therefore reduced, but still visible. Figure 3d shows the corresponding height profile of the PMMA through the centre of the lens. Clearly visible are the three gold ridges for launching the SPPs at $z = 0$ μm and the linear height change of the Luneburg lens.

Although the Luneburg lens was designed for a particular wavelength of 800 nm, the dispersion of the PMMA around this wavelength is reasonably small. Therefore, the dispersion of SPPs due to the different penetration into the dielectric medium is not affected by the PMMA. All three wavelengths in Fig. 3a–c show clear focusing, although for longer wavelengths the focus is shifted slightly behind the lens. Such behaviour for longer wavelengths is mainly due to the larger penetration depth of the SPP field into the dielectric material. As a result, the overall effective mode index is smaller than that required for an ideal Luneburg lens (see equation (1)), so the effective focal length is slightly longer. Nevertheless, the Luneburg lens shows good performance within the measured 70 nm bandwidth.

To demonstrate the versatility of our method to create low-loss manipulation of SPPs solely by gradually tailoring the dielectric cladding layer, a plasmonic Eaton lens was designed and experimentally demonstrated. The index distribution of a perfect Eaton lens that bends light through 90° satisfies[30]

$$n^2 = \frac{R}{nr} + \sqrt{\left(\frac{R}{nr}\right)^2 - 1} \qquad (2)$$

Unlike the Luneburg lens, the refractive index quickly diverges towards the centre of the Eaton lens. As the coating with PMMA can provide only a limited mode index range for SPPs from 1.02 up to 1.54, we were not able to realize the central part of the Eaton lens. For practical purposes, we therefore truncate the index profile at a maximum of 1.54, as shown in Fig. 4a.

A numerical simulation of SPP propagation for the truncated Eaton lens is shown in Fig. 4b. The excited SPPs are propagating in the positive z-direction and bend to the right side while passing through the lens. Eventually, SPPs leave the structure in the positive x-direction. Owing to the inherent propagation loss of SPPs, the field magnitude decreases during propagation. Truncation of the index in the centre part of the lens leads to a small deviation from the perfect

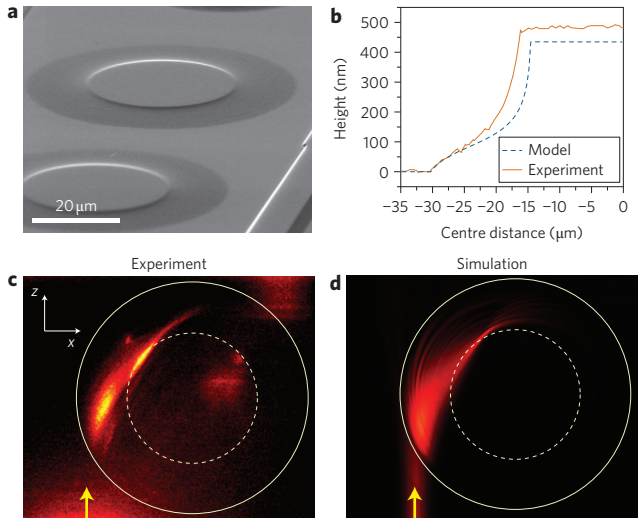

Figure 5 | Demonstration of a plasmonic Eaton lens. a, SEM image of an array of Eaton lenses on top of a gold film. **b**, Height profile cross-section for the left side of the lens measured by AFM (solid line) compared to the model (dashed line). **c**,**d**, Fluorescence microscopy image and corresponding simulation of the fluorescence intensity of the Eaton lens for SPPs propagating in the positive *z*-direction and bending to the right side when passing through the lens. Arrows indicate the launching position and direction of the SPPs. Solid lines mark the outer diameter of the lens and dashed lines the high index region, which was set to 1.54. In the colour scale, black represents low intensities and yellow high intensities.

90° bend. To extract the influence of the changing field magnitude we again calculate the corresponding fluorescence intensity by taking the local thickness of the PMMA into account (Fig. 4c).

A scanning electron microscopy image of the structure is shown in Fig. 5a, together with the corresponding cross-section of the height profile (Fig. 5b). Although the profile is more complex than that of the Luneburg lens, the overall agreement is reasonably good; only the steepest part of the profile shows a small discrepancy from the theoretical model, probably due to proximity effects during exposure. The SPP-induced fluorescence emission intensity from the structure is shown in Fig. 5c, where the SPPs are propagating from the bottom in the positive *z*-direction and bend inside the Eaton lens to the right side. Figure 5d shows the simulated fluorescence intensity for the actual PMMA profile of the lens measured by AFM. Both images show similar features as the simulation carried out for the ideal profile (Fig. 4c).

In summary, we have experimentally demonstrated the feasibility of tailoring the propagation of SPPs by solely modifying a dielectric material on top of a metal. Because the topology of the dielectric structure is slowly varied, this technique is analogous to the well-known gradient index optics. Owing to the penetration depth of the evanescent SPP field into the dielectric material, the propagation constant can be spatially and gradually modified with different thicknesses of a dielectric index material. We have demonstrated our approach for a plasmonic Luneburg lens and an Eaton lens, neither of which have been demonstrated at optical frequencies to date. Our approach has the potential to achieve low-loss functional plasmonic elements with a standard fabrication technology based on grey-scale EBL and is fully compatible with active plasmonics. The loss could be reduced even further by incorporating various gain materials into the dielectric material[34], leading to the increased propagation distance required for all-optical devices or even plasmonic interconnects. Furthermore, this method provides a scheme with which to realize more complex two-dimensional plasmonic elements using transformation optics.

Methods

The grey-scale EBL process began by determining the relationship between PMMA resist height and dose value. To enable precise control over the resist height, low-contrast 50k PMMA was used, allowing a more linear resist response with respect to dose. The correlation between height and dose was then used to determine the spatially varying dose profile for the designed height/index profile. Devices for fluorescence emission imaging were fabricated by incorporating infrared dye (IR-140, Sigma Aldrich) into the PMMA at a loading concentration of 2 mg dye to 1 ml PMMA. The dye/PMMA solution was spun and baked onto a 200-nm-thick gold film on top of a glass substrate, resulting in a thickness of 500 nm. Grey-scale EBL exposure was then performed to realize the designed height profile for the Luneburg and Eaton lenses.

For our design and simulations, we used as the dielectric cladding layer PMMA with $\varepsilon_2 = 2.19$ on top of a gold film, for which the dielectric constants are given by the Drude model $\varepsilon_m(\omega) = 10 - ((1.4 \times 10^{16})^2/\omega(\omega + 1.1 \times 10^{14}i))$. Considering an air/dielectric/metal structure with permittivities $\varepsilon_1/\varepsilon_2/\varepsilon_m$, the dispersion relation of SPPs is implicitly given by[27]

$$\tanh(k_2\varepsilon_2 d) = -\frac{k_1 k_2 + k_2 k_m}{k_2^2 + k_1 k_m}$$

with

$$k_{1(2,m)} = \frac{\sqrt{\beta^2 - \varepsilon_{1(2,m)}\omega^2/c^2}}{\varepsilon_{1(2,m)}}$$

Here, d is the thickness of the dielectric layer, β represents the SPP wave vector along the propagating direction, ω is angular frequency, and c denotes the speed of light in vacuum. The effective mode index of SPPs, defined as $n_{\mathrm{eff}} = \beta/k_0$, can be obtained by numerically solving the above two equations for different heights of the dielectric layer. Once the relationship between the SPP effective index and the PMMA height is known, the PMMA profile for the plasmonic Luneburg and Eaton lenses can be readily achieved to satisfy equations (1) and (2), respectively.

For the fluorescence imaging measurements, SPPs were launched by a set of gratings fabricated by focused ion beam milling, at a distance of 10 μm from the lens structure. Light from a Ti:sapphire laser at a wavelength of 810 nm was moderately focused on the grating from the backside of the sample to a spot size of 6 μm. The fluorescence emission from the IR140 dye molecules was collected with a ×100/0.95 microscope objective and imaged on a charge-coupled device camera.

For the leakage radiation microscopy experiment, SPPs were launched by three gold ridges with a period of 805 nm and a line width of 400 nm fabricated by EBL and subsequent deposition of 50 nm gold[33]. SPPs were launched by focusing the laser light with a microscope objective (×10/0.1) on these gold ridges. The leakage radiation of the SPPs into the substrate was collected by an oil immersion objective (×100/1.3) and imaged on a charge-coupled device camera.

Received 5 November 2010; accepted 21 December 2010; published online 23 January 2011

References

1. Barnes, W. L., Dereux, A. & Ebbesen, T. W. Surface plasmon subwavelength optics. *Nature* **424,** 824–830 (2003).
2. Nie, S. M. & Emery, S. R. Probing single molecules and single nanoparticles by surface-enhanced Raman scattering. *Science* **275,** 1102–1106 (1997).
3. Fang, N., Lee, H, Sun, C. & Zhang, X. Sub-diffraction-limited optical imaging with a silver superlens. *Science* **308,** 534–537 (2005).
4. Stockman, M. I. Nanofocusing of optical energy in tapered plasmonic waveguides. *Phys. Rev. Lett.* **93,** 137404 (2004).
5. Srituravanich, W. *et al.* Flying plasmonic lens in the near field for high-speed nanolithography, *Nature Nanotech.* **3,** 733–737 (2008).
6. Hohenau, A. *et al.* Dielectric optical elements for surface plasmons. *Opt. Lett.* **30,** 893–895 (2005).
7. Bozhevolnyi, S. I., Volkov, V. S., Devaux, E., Laluet, J.-Y. & Ebbesen, T. W. Channel plasmon subwavelength waveguide components including interferometers and ring resonators. *Nature* **440,** 508–511 (2006).
8. Drezet, A. *et al.* Plasmonic crystal demultiplexer and multiports. *Nano Lett.* **7,** 1697–1700 (2007).
9. Engheta, N. Circuits with light at nanoscales: optical nanocircuits inspired by metamaterials. *Science* **317,** 1698–1702 (2007).
10. Oulton, R. F. *et al.* Plasmon lasers at deep subwavelength scale. *Nature* **461,** 629–632 (2009).
11. Bozhevolnyi, S. I., Erland, J., Leosson, K., Skovgaard, P. M. W. & Hvam, J. M. Waveguiding in surface plasmon polariton band gap structures. *Phys. Rev. Lett.* **86,** 3008–3011 (2001).

12. Ditlbacher, H., Krenn, J. R., Schider, G., Leitner, A. & Aussenegg, F. R. Two-dimensional optics with surface plasmon polaritons. *Appl. Phys. Lett.* **81,** 1762–1764 (2002).
13. Smolyaninov, I. I., Elliott, J., Zayats, A. V. & Davis, C. C. Far-field optical microscopy with a nanometer-scale resolution based on the in-plane image magnification by surface plasmon polaritons. *Phys. Rev. Lett.* **94,** 057401 (2005).
14. Devaux, E. *et al.* Refractive micro-optical elements for surface plasmons: from classical to gradient index optics. *Opt. Express* **18,** 20610–20619 (2010).
15. Smolyaninov, I. I. Transformational optics of plasmonic metamaterials. *New J. Phys.* **10,** 115033 (2008).
16. Pendry, J. B., Schurig, D. & Smith, D. R. Controlling electromagnetic fields. *Science* **312,** 1780–1782 (2006).
17. Leonhardt, U. Optical conformal mapping. *Science* **312,** 1777–1780 (2006).
18. Schurig, D. *et al.* Metamaterial electromagnetic cloak at microwave frequencies. *Science* **314,** 977–980 (2006).
19. Valentine, J., Li, J., Zentgraf, T., Bartal, G. & Zhang, X. An optical cloak made of dielectrics. *Nature Mater.* **8,** 568–571 (2009).
20. Gabrielli, L. H., Cardenas, J., Poitras, C. B. & Lipson, M. Silicon nanostructure cloak operating at optical frequencies. *Nature Photon.* **43,** 461–463 (2009).
21. Cheng, Q., Cui, T. J., Jiang, W. X. & Cai, B. G. An omnidirectional electromagnetic absorber made of metamaterials. *New J. Phys.* **12,** 063006 (2010).
22. Zentgraf, T., Valentine, J., Tapia, N., Li, J. & Zhang, X. An optical 'Janus' device for integrated photonics. *Adv. Mater.* **22,** 2561–2564 (2010).
23. Kundtz, N. & Smith, D. R. Extreme-angle broadband metamaterial lens. *Nature Mater.* **9,** 129–132 (2010).
24. Luneburg, R. *Mathematical Theory of Optics* (Brown University, 1944).
25. Eaton, J. E. On spherically symmetric lenses. *Trans. IRE Antennas Propag.* **4,** 66–71 (1952).
26. Huidobro, P. A., Nesterov, M. L., Martín-Moreno, L. & García-Vidal, F. J. Transformation optics for plasmonics. *Nano Lett.* **10,** 1985–1990 (2010).
27. Liu, Y., Zentgraf, T., Bartal, G. & Zhang, X. Transformational plasmon optics. *Nano Lett.* **10,** 1991–1997 (2010).
28. Renger, J. *et al.* Hidden progress: broadband plasmonic invisibility. *Opt. Express* **18,** 15757–15768 (2010).
29. Aubry, A. *et al.* Plasmonic light-harvesting devices over the whole visible spectrum. *Nano Lett.* **10,** 2574–2579 (2010).
30. Danner, A. J. & Leonhardt, U. Lossless design of an Eaton lens and invisible sphere by transformation optics with no bandwidth limitation *Conference on Lasers and Electro-Optics* (CLEO), Baltimore, MD, USA, 31 May–5 June 2009.
31. Ditlbacher, H. *et al.* Fluorescence imaging of surface plasmon fields. *Appl. Phys. Lett.* **80,** 404–406 (2002).
32. Drezet, A. *et al.* Leakage radiation microscopy of surface plasmon polaritons. *Mater. Sci. Eng. B* **149,** 220–229 (2008).
33. Radko, I. P. *et al.* Effciency of local surface plasmon polariton excitation on ridges. *Phys. Rev. B* **78,** 115115 (2008).
34. De Leon, I. & Berini, P. Amplification of long-range surface plasmons by a dipolar gain medium. *Nature Photon.* **4,** 382–387 (2010).

Acknowledgements

The authors acknowledge funding support from the US Army Research Office (MURI programme W911NF-09-1-0539) and the US National Science Foundation (NSF Nanoscale Science and Engineering Center CMMI-0751621).

Author contributions

T.Z., Y.L. and J.V. conceived and designed the experiments. T.Z. and M.H.M. performed the experiments and analysed the data. Y.L. designed the structures and performed the numerical simulations. J.V. and M.H.M. fabricated the samples. X.Z. guided the theoretical and experimental work. All authors discussed the results and co-wrote the manuscript.

Additional information

The authors declare no competing financial interests. Reprints and permission information is available online at http://npg.nature.com/reprintsandpermissions/. Correspondence and requests for materials should be addressed to X.Z.